

THREE-DIMENSIONAL AERODYNAMIC ANALYSIS OF A WING–ROTOR CONFIGURATION FOR A FOLDING WING UAV

Seunghyun Choi[1], Yoosang Lee[1], Huichan Choi[2], Byeonggeun Cho[2], Youngruun Kim[1] & Dongwon Jung[1]

[1]Department of Smart Air Mobility, Korea Aerospace University
[2]Department of Mechanical Engineering, Korea Aerospace University

Abstract

The growing demand for Urban Air Mobility (UAM) has driven the development of electric vertical takeoff and landing (eVTOL) aircraft configurations that combine vertical lift capability with efficient cruise performance. Among these configurations, Folding wing designs offer a promising balance between compact stowage and aerodynamic performance. However, these designs introduce complex rotor–wing aerodynamic interactions during transition flight, posing significant modeling challenges. While high-fidelity computational fluid dynamics (CFD) and wind-tunnel testing can capture these effects, they are often impractical for early-stage design due to cost and time constraints. To address this challenge, this study develops a physics-based aerodynamic modeling approach for a Folding wing UAV. The aerodynamic model couples three-dimensional Blade Element Momentum Theory (BEMT) with a spanwise strip-theory wing model to estimate rotor-wing interference, non-axial inflow, and wing aerodynamic loads. The resulting forces and moments are integrated into a six-degree-of-freedom (6-DOF) trim formulation that accounts for changes in center of gravity (CG) and inertia resulting from wing articulation. Trim solutions are obtained across hover, transition, and cruise. The resulting framework unifies aerodynamic and propulsive analysis across flight regimes and provides a computationally efficient tool for early-stage evaluation of Folding wing UAV configurations without requiring wind-tunnel-based calibration.

Keywords: Folding wing, BEMT, Rotor-wing interference, Aerodynamic modeling, Transition flight

1. Introduction

The growing demand for Urban Air Mobility (UAM) has driven the rapid development of electric vertical takeoff and landing (eVTOL) aircraft that combine vertical lift capability with efficient cruise performance. To meet these competing requirements, various configurations have been explored, including powered-lift, vectored-thrust, tilt-prop, and tilt-wing designs. Recent prototypes highlight the diversity of design approaches: Joby Aviation's S4 is classified as a powered-lift eVTOL aircraft with a vectored-thrust tilt-prop configuration [1], while NASA has tested subscale tilt-wing concepts such as the GL-10 UAV [2] and the LA-8 tandem tilt-wing testbed [3].

Among these architectures, Folding wing configurations offer a promising balance between compact stowage and aerodynamic performance, supporting VTOL operation while improving efficiency in forward flight [4]. However, wing articulation alters the relative arrangement of rotors and lifting surfaces, introducing complex rotor–wing aerodynamic interactions during transition flight and posing significant modeling challenges. Such coupling can produce nonlinear and configuration-dependent flow effects that are difficult to capture with conventional decoupled rotor or wing models.

Empirical methods, including wind tunnel and flight tests such as NASA's LA-8, offer validation data but are costly and time-intensive. Other experimental efforts involving morphing-wing UAV experiments [5] have advanced understanding but still underscore the limitations of being purely empirical or high-fidelity simulations at the early design stage.

To address this challenge, this study presents a physics-based aerodynamic modeling approach tailored to a Folding wing UAV. The modeling architecture integrates three components. First, a three-dimensional Blade Element Momentum Theory (BEMT) module computes rotor forces under non-axial inflow by discretizing blades into radial elements. Second, a spanwise strip-theory module captures rotor–wing interference by iteratively updating panel circulation while accounting for upstream slipstream effects. Third, an adaptive trim solver embeds these aerodynamic models within six-degree-of-freedom (6-DOF) equations of motion and applies regime-dependent control allocation, from differential thrust in hover to aerodynamic surfaces in cruise, to compute equilibrium across the transition envelope. This approach enables prediction of rotor–wing interference and non-axial inflow while accounting for configuration-dependent variations in center of gravity (CG) and inertia resulting from wing articulation. By unifying aerodynamic and propulsive analyses across flight regimes without relying on wind-tunnel-based calibration, the proposed framework provides a computationally efficient and scalable tool for early-stage evaluation of Folding wing UAV configurations.
The transition process of the Folding wing UAV is illustrated in Fig. 1, where the configuration gradually morphs from the multicopter mode to the fixed-wing mode as the wing pivots.

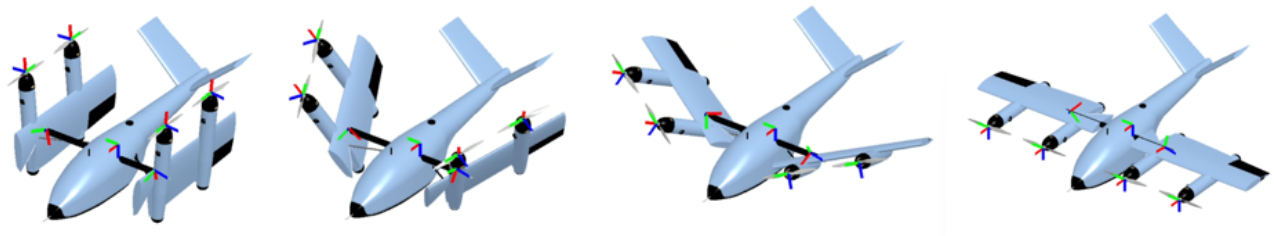


Figure 1 – Transition process of the Folding wing UAV

2. METHODOLOGY

2.1 Coordinate Frame Definitions and Transformation

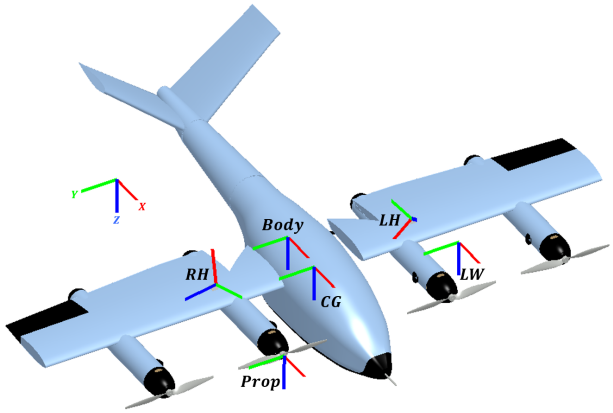


Figure 2 – Coordinate system of the Folding wing in the body frame

The body frame B is defined at the center of gravity (CG) of the fuselage and vertical tail, excluding the wings. The hinge frames LH and RH are introduced to represent the wing kinematics, where a rotation about the local Z-axis describes the wing rotation through the pivot angle γ_p. The wing frames LW and RW are defined at the respective wing centers of gravity and serve as the reference for aerodynamic force and moment calculations. The overall configuration of these coordinate frames is illustrated in Fig. 2.
Transformations from the body frame to the hinge frame, and subsequently from the hinge frame to the wing frame, are represented using an intrinsic Z–X–Y Euler rotation sequence. The pivot angle γ_p specifies the wing rotation, where $\gamma_p = 0^\circ$ corresponds to the multicopter configuration and $\gamma_p = 117^\circ$

represents the fixed-wing configuration. Accordingly, the body-to-wing transformation is expressed as

$$T_B^{RW} = T_{RH}^{RW}\ T_B^{RH}, \quad T_B^{LW} = T_{LH}^{LW}\ T_B^{LH} \tag{1}$$

where T_{RH}^{RW} and T_{LH}^{LW} represent the transformations from each hinge frame to the corresponding wing frame. Similarly, the body-to-propeller transformations are defined as $T_B^{RP_i}$ and $T_B^{LP_i}$. These can be expressed in mathematical form as

$$T_B^{RP_i} = T_{RH}^{RP_i}\ T_B^{RH}, \quad T_B^{LP_i} = T_{LH}^{LP_i}\ T_B^{LH} \tag{2}$$

The thrust axes are defined along the local x-axis of each propeller frame. As shown in Fig. 2, the numbering convention is defined as P_1 = Right Inner, P_4 = Right Outer, P_2 = Left Outer, P_3 = Left Inner.

2.2 Dynamic Modeling of the Folding wing UAV

The Folding wing UAV is modeled as a rigid body governed by the 6-DOF equations of motion in the body-fixed frame. A general formulation of the 6-DOF dynamics and the associated kinematics can be found in the literature [6]. The total forces and moments acting on the UAV can be expressed as

$$\sum F = m\dot{V}_B + m\,\omega_B \times V_B \tag{3}$$

$$\sum M = I\dot{\omega}_B + \omega_B \times (I\omega_B) \tag{4}$$

where m is the total mass, V_B the velocity in the body frame, ω_B the angular velocity, and I the inertia tensor.

The total external force acting on the vehicle is decomposed into gravitational, aerodynamic, and thrust contributions:

$$\sum F = F_g + F_{\text{aero}} + F_{\text{thr}} \tag{5}$$

Here, F_g represents the gravitational force resolved in the CG frame, F_{aero} is the resultant of aerodynamic loads from the wings and tail surfaces, and F_{thr} accounts for propulsive forces generated by the distributed propeller system. The corresponding moment decomposition follows analogously, incorporating contributions from aerodynamic moments, propeller-induced moments, and gyroscopic moments. The angular momentum balance is formulated as

$$\sum M = M_{\text{gyro}} + M_{\text{aero}} + M_{\text{thr}} \tag{6}$$

These formulations provide the foundation for analyzing the coupled dynamics of the Folding wing UAV across hover, transition, and fixed-wing flight regimes.

2.3 Center of Gravity and Inertia Tensor

The Folding wing UAV incorporates batteries and actuators inside the wings, which causes both the center of gravity (CG) location and the inertia tensor to vary with the wing pivot angle. The derivation follows the parallel–axis theorem and tensor shift method [7].

Total mass and CG in the body frame: The total mass of the UAV is obtained as the sum of the fuselage (Fuse), right wing (RW), and left wing (LW) components

$$m_{\text{tot}} = m_{\text{Fuse}} + m_{\text{RW}} + m_{\text{LW}} \tag{7}$$

The weighted sum of the position vectors of each component with respect to the body frame can then be written as

$$r^* = m_{\text{Fuse}}\, r_{B\to Fuse} + m_{\text{RW}}\, r_{B\to RW} + m_{\text{LW}}\, r_{B\to LW} \tag{8}$$

As shown in (8), the term $m_{\text{Fuse}}\, r_{B\to\text{Fuse}}$ vanishes since the body-frame origin is defined to coincide with the fuselage reference point such that $r_{B\to\text{Fuse}} = 0$.

Finally, the position of the center of gravity (CG) relative to the body frame is obtained by normalizing this weighted sum with the total mass

$$r_{B\to CG} = \frac{r^*}{m_{\text{tot}}} \tag{9}$$

The parallel–axis increment can be written in compact form as

$$\Delta J^{F}_{p\to q} = m\left(\|r_{p\to q}\|^2 I_3 - r_{p\to q} r^T_{p\to q}\right) \tag{10}$$

where $p \to q$ indicates the shift of the reference point from p to q, and the superscript F denotes the frame in which the tensor is expressed. The scalar m corresponds to the part mass when $p \to q$ refers to a part-to-body shift, and to the total mass m_{tot} when $p \to q$ denotes the body-to-CG shift.
In the notation ${}^{B}J_{(\cdot)}$, the superscript B indicates that the tensor is expressed in the body-fixed frame, while the subscript specifies the reference point about which the inertia is taken, such as c_i, B, or CG.
Rotation from local to body frame For each component $i \in \{\text{Fuse}, \text{RW}, \text{LW}\}$ with centroid c_i, the inertia about c_i expressed in the body frame is

$${}^{B}J_{c_i} = C_i^B \, {}^{i}J_{c_i} \, (C_i^B)^T \tag{11}$$

Parallel–axis shift from centroid to body origin

$${}^{B}J_{B,i} = {}^{B}J_{c_i} + \Delta J^{B}_{i\to B} \tag{12}$$

Total inertia tensor at the body origin

$${}^{B}J_{B} = {}^{B}J_{B,Fuse} + {}^{B}J_{B,RW} + {}^{B}J_{B,LW} \tag{13}$$

Here the fuselage has its centroid coincident with the body origin, so that $\Delta J^{B}_{Fuse\to B} = 0$. Shift from body origin to CG Since the body-fixed frame and the CG frame are aligned in orientation, ${}^{CG}J_B$ is equivalent to ${}^{B}J_B$. Hence, the inertia tensor about the CG can be written as

$${}^{CG}J_{CG} = {}^{CG}J_B + \Delta J^{CG}_{B\to CG} \tag{14}$$

2.4 3D-Blade Element Momentum Theory

The BEMT is employed to model the propeller aerodynamics in the presence of non-axial inflow induced by wing pivoting [8]. For a given pivot angle, the freestream velocity is decomposed into axial and radial components, and the resulting blade element contributions are integrated over the azimuth to obtain cycle-averaged forces and moments. Specifically, integration over the azimuth angle yields the average elemental loads, where $d\vec{F}_{avg}$ and $d\vec{M}_{avg}$ denote the elemental forces and moments averaged over one rotor revolution. The aggregated results yield the propeller thrust and torque, which are obtained in accordance with standard conventions in propeller aerodynamics [9].

$$\vec{F}^{bemt}_{thr} = \int d\vec{F}_{avg} = \begin{Bmatrix} \vec{F}_x \\ 0 \\ \vec{F}_z \end{Bmatrix} \tag{15}$$

$$\vec{M}^{bemt}_{thr} = \int d\vec{M}_{avg} = \begin{Bmatrix} \vec{M}_x \\ 0 \\ \vec{M}_z \end{Bmatrix} \tag{16}$$

As the wing pivots during transition, the advance ratio λ varies accordingly and is evaluated at each pivot angle to capture the changing inflow condition.
As illustrated in Fig. 3, the BEMT formulation is derived under the assumption that the freestream velocity lies in the xz plane. To satisfy this condition, the original propeller coordinate system is rotated by an angle θ_{prop} such that the freestream velocity vector aligns with the new z-axis. Let the orthonormal basis vectors of the original propeller frame be $(\hat{x}_p, \hat{y}_p, \hat{z}_p)$. After the rotation, the new z-axis, denoted as $\hat{z}'_p$, must lie in both the plane spanned by $\hat{y}_p$ and $\hat{z}_p$ and the plane spanned by $\hat{x}_p$ and $\vec{V}$. Therefore, it can be expressed as a linear combination

$$\hat{z}'_p = \alpha_n \hat{x}_p + \beta_n \vec{V}, \quad \hat{z}'_p \cdot \hat{x}_p = 0 \tag{17}$$

where α_n and β_n denote arbitrary constants constrained by the orthogonality condition. which leads to

$$(\alpha_n \hat{x}_p + \beta_n \vec{V}) \cdot \hat{x}_p = \alpha_n + \beta_n (\vec{V} \cdot \hat{x}_p) = 0 \tag{18}$$

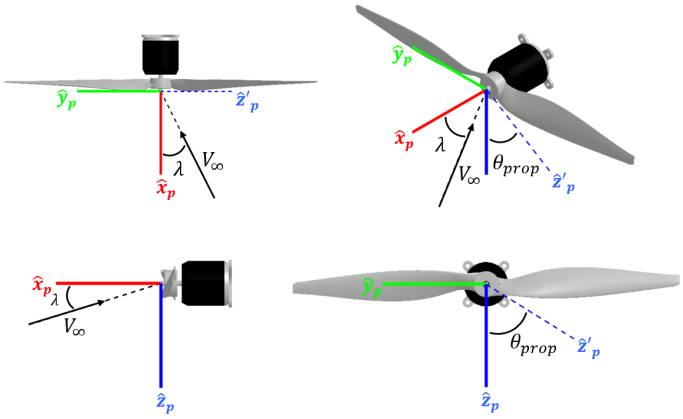


Figure 3 – Propeller Coordinate System for BEMT

and hence $\alpha_n = -\beta_n(\vec{V}\cdot\hat{x}_p)$. Substituting this result yields

$$\hat{z}'_p = -\beta_n(\vec{V}\cdot\hat{x}_p)\hat{x}_p + \beta_n\vec{V} = \beta_n(0, V_y, V_z) \tag{19}$$

Accordingly, the required rotation transformation C_{bemt}^{prop} is defined as a rotation about the x-axis by the angle θ_{prop}, enabling the forces and moments obtained from the BEMT calculation to be expressed in the original propeller frame for consistent force and moment summation in the body frame.

$$\begin{aligned} \vec{F}_{thr}^{prop} &= C_{bemt}^{prop}\,\vec{F}_{thr}^{bemt} \\ \vec{M}_{thr}^{prop} &= C_{bemt}^{prop}\,\vec{M}_{thr}^{bemt} \end{aligned} \tag{20}$$

The rotation matrices from each propeller to the body frame, $C_B^{RP_i}$ and $C_B^{LP_i}$ are defined as the rotational components of the homogeneous matrix given in Eq. (6). Since the center-of-gravity (CG) frame and the body frame are aligned, the rotation between the CG and the body frame reduces to the identity, and thus the rotations with respect to the CG are equivalent to those with respect to the body frame. Accordingly, the propeller forces expressed at the CG can be written as

$$F_{thr,i}^{CG} = \begin{cases} C_{RP_i}^{CG} F_{thr,i}^{prop} & (i = 1,4) \\ C_{LP_i}^{CG} F_{thr,i}^{prop} & (i = 2,3) \end{cases} \tag{21}$$

The moments generated by the propellers about the center of gravity (CG) consist of two components: the intrinsic moments produced by the propellers themselves and the additional moments induced by the moment arm due to their offset from the CG. Among these, the moment induced by the arm can be expressed as follows

$$M_{r\times F_{thr,i}}^{CG} = \begin{cases} r_{CG\to RP_i} \times F_{thr,i}^{CG} & (i = 1,4) \\ r_{CG\to LP_i} \times F_{thr,i}^{CG} & (i = 2,3) \end{cases} \tag{22}$$

This term is expressed as the cross product between the position vector and the thrust force, and the thrust moment about the CG is defined as

$$M_{thr,i}^{CG} = \begin{cases} C_{RP_i}^{CG} M_{thr,i} + M_{r\times F_{thr,i}}^{CG} & (i = 1,4) \\ C_{LP_i}^{CG} M_{thr,i} + M_{r\times F_{thr,i}}^{CG} & (i = 2,3) \end{cases} \tag{23}$$

Accordingly, the thrust-induced forces and moments in the CG frame can be expressed as follows.

$$F_{thr} = \sum_{i=1}^{4} F_{thr,i}^{CG} \quad M_{thr} = \sum_{i=1}^{4} M_{thr,i}^{CG} \tag{24}$$

2.5 Aerodynamic Modeling

Using lifting-line theory with circulation-based corrections, the post-stall behavior is approximated by a normal-force model relating force coefficient to angle of attack. The corresponding lift and drag components are obtained by resolving this normal force into axial and transverse directions. This approach is consistent with the widely used thin-airfoil post-stall approximation, as detailed in [10, 11], and provides a simple yet effective means to capture the highly nonlinear aerodynamics beyond the stall regime without relying on extensive empirical data.

The increment of the axial velocity in the propeller slipstream can be obtained from the actuator-disk momentum balance, while the treatment of slipstream effects is discussed in the literature [12].

$$w = \frac{1}{2}\left(-V_{wing,x} + \sqrt{(V_{wing,x})^2 + \frac{2T}{\rho A}}\right) \tag{25}$$

where T is the propeller thrust, ρ is the air density, and A is the propeller disk area.

$$V_\infty = \sqrt{(2w + V_{wing,x})^2 + (V_{wing,z})^2} \tag{26}$$

According to momentum theory, the induced velocity in the slipstream converges to $2w$. Consequently, the resultant velocity in the wing frame represents the combined effect of the freestream and the slipstream-induced component.

$$\alpha_s = \arctan\left(\frac{V_{wing,z}}{2w + V_{wing,x}}\right) \tag{27}$$

The effective angle of attack of the wing, accounting for the influence of the slipstream, denotes the modified incidence used in the aerodynamic model. In strip theory, each lifting surface is discretized

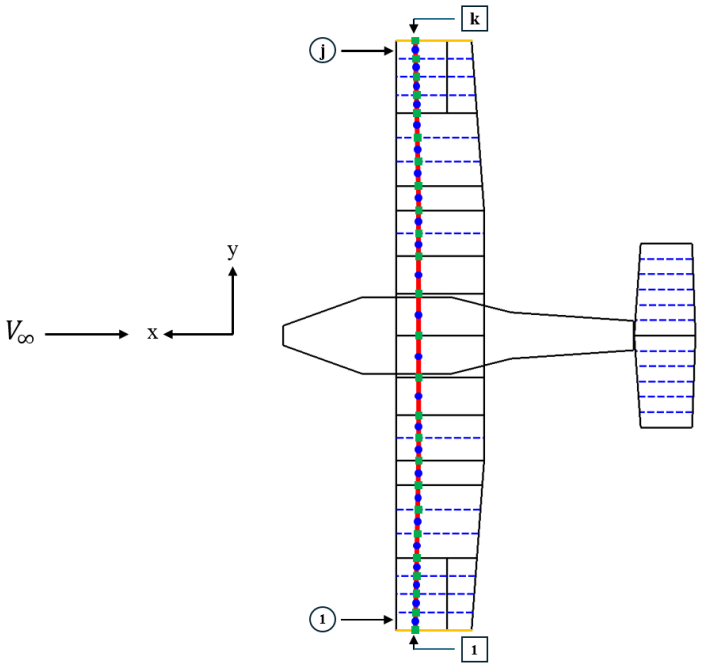


Figure 4 – Fixed-Wing Configuration and Lifting-Line Panels

into spanwise sections, and the sectional forces are integrated to obtain the overall aerodynamics [13]. For the wing and tail, the numbers of panels are n_p and n_{Tp}, giving $k_w = n_p + 1$ and $k_t = n_{Tp} + 1$ boundary points.

As shown in Fig. 4, the black solid lines indicate the aileron positions, the region between the thrust lines, the tapered section, and the wing root. The blue dashed lines represent the subdivision of these black solid lines into equal segments. The orange solid lines denote the shed vortices generated at

the wing tips. Finally, the red solid line corresponds to the quarter–chord line along the span, on which the blue circles indicate the aerodynamic force application points $(x_{LLT_j}, y_{LLT_j}, z_{LLT_j})$, while the green squares represent the panel boundary points $(x_{PS_k}, y_{PS_k}, z_{PS_k})$. The initial bound circulation at section j is

$$\Gamma_{0_j} = \frac{1}{2} V_{\infty_j} \bar{c}_j C_{l_j} \tag{28}$$

where V_{∞_j} is the local velocity, $\bar{c}_j$ the chord, and C_{l_j} the sectional lift coefficient. As shown in Fig. 5,the effective angle of attack is

$$\alpha_{eff_j} = \alpha_{geo_j} - \alpha_{ind_j} \tag{29}$$

with α_{geo_j} from Eq. (27) and α_{ind_j} updated iteratively.
The circulation at each lifting-line control point is

$$\Gamma_{LLT_j} = \frac{1}{2} \left(\Gamma_{init_j} + \Gamma_{init_{j+1}} \right) \tag{30}$$

where the initial estimate is

$$\Gamma_{init_j} = \Gamma_{0_j} \sqrt{1 - \left(\frac{2y_j}{b} \right)^2} \tag{31}$$

The shed circulation between panels is defined as

$$\begin{aligned} \Gamma_{SV_1} &= \Gamma_{LLT_1} \\ \Gamma_{SV_j} &= \Gamma_{LLT_j} - \Gamma_{LLT_{j-1}} \\ \Gamma_{SV_{n_p}} &= -\Gamma_{LLT_{n_p+1}} \end{aligned} \tag{32}$$

where the negative sign accounts for the free-end effect. The induced downwash at control point j due to vortex segment k is

$$w_{ind_{j_k}} = \frac{\Gamma_{SV_k}}{4\pi} \frac{-\Delta y_{j_k}}{(\Delta z_{j_k})^2 + (\Delta y_{j_k})^2} \left(1 + \frac{\Delta x_{j_k}}{R_{j_k}} \right) \tag{33}$$

with $R_{j_k} = \sqrt{(\Delta x_{j_k})^2 + (\Delta y_{j_k})^2 + (\Delta z_{j_k})^2}$. Finally, the total downwash at j is the superposition

$$w_{ind_j} = \sum_{k=1}^{n_p+1} w_{ind_{j_k}} \tag{34}$$

The induced angle of attack and relative velocity at each lifting-line point are

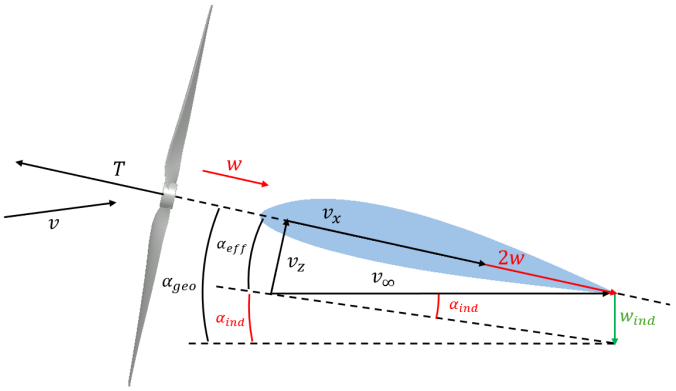


Figure 5 – Induced Velocities in the Propeller Slipstream

$$\alpha_{ind_j} = \arctan\left(-\frac{w_{ind_j}}{V_{\infty j}} \right), V_{rel_j} = \sqrt{V_{\infty j}^2 + w_{ind_j}^2} \tag{35}$$

The sectional normal force can be expressed either from lift,

$$N'_j = \frac{L'_j}{\cos(\alpha_{ind_j})}, L'_j = \tfrac{1}{2}\rho V_{\infty_j}^2 \bar{c}_j C_{l_j} \tag{36}$$

or equivalently from circulation

$$N'_j = \rho\, V_{rel_j} \Gamma_{LLT_j} \tag{37}$$

The circulation update from lifting-line theory is

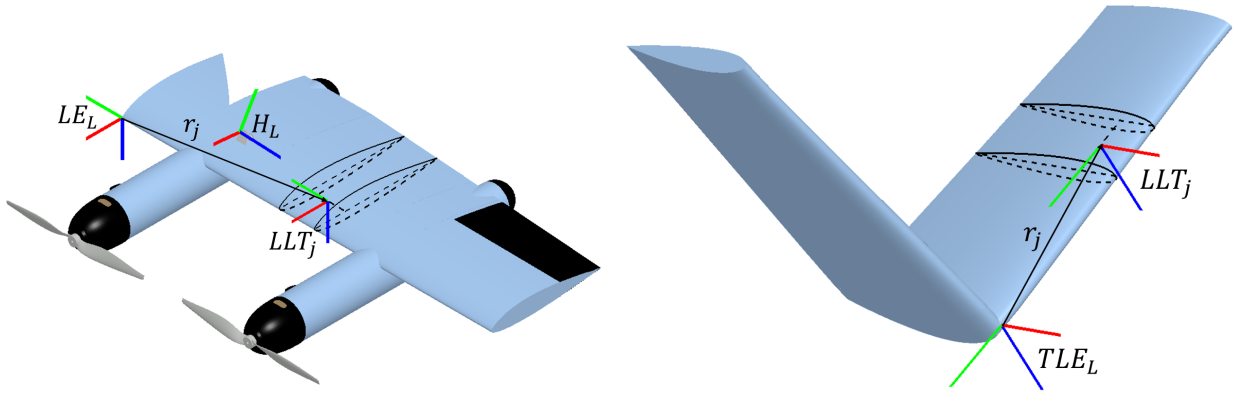
$$\Gamma_{LLT,new_j} = \tfrac{1}{2} \frac{V_{\infty j}^2}{V_{rel_j}} \cos(\alpha_{ind_j})\, \bar{c}_j C_{l_j} \tag{38}$$

with under-relaxation applied for stability:

$$\Gamma_{LLT_j} = D\Gamma_{LLT,new_j} + (1-D)\Gamma_{LLT_j} \tag{39}$$

where the damping factor D is typically chosen between 0.05 and 0.1. Convergence is reached when

$$\tfrac{1}{n_p} \sum_{j=1}^{n_p} \left(\Gamma_{LLT,new_j} - \Gamma_{LLT_j}\right)^2 \leq 10^{-5} \tag{40}$$



(a) Wing lifting-line coordinate

(b) V-tail lifting-line coordinate

Figure 6 – Coordinate system definitions for (a) wing and (b) V-tail lifting-line

Each wing LLT$_j$ frame is obtained by applying the transform with respect to the leading edge, combined with the translation matrix in Eq. (42). In this equation, r_j^{LW} and r_j^{RW} represent the distance vectors from the leading edge to the LLT in the left and right wings (or tail), respectively. The resulting frame provides the global mapping of aerodynamic control points in Eq. (43), as illustrated in Fig. 6.

$$T_B^{LE_L} = T_{LH}^{LE_L} T_B^{LH}, \quad T_B^{LE_R} = T_{RH}^{LE_R} T_B^{RH} \tag{41}$$

$$T_{LE}^{LLT_j} = \begin{cases} \begin{bmatrix} I_3 & r_j^{LW} \\ 0 & 1 \end{bmatrix}, & j = 1, \ldots, \frac{n_p}{2} \\ \begin{bmatrix} I_3 & r_j^{RW} \\ 0 & 1 \end{bmatrix}, & j = \frac{n_p}{2}+1, \ldots, n_p \end{cases} \tag{42}$$

$$T_B^{LLT_j} = T_{LE}^{LLT_j} T_B^{LE} \tag{43}$$

In the transition region, vortices are assumed to originate near the wing root, as illustrated in Fig. 7. Since this model may overemphasize the wing-root vortex, the circulation from the fixed-wing state to about 20° pivot angle is blended with the fixed-wing results. Moreover, unlike conventional aircraft that use the Body frame, here the flow velocity and geometric angle of attack α_{geo} are defined in the Wing frame.

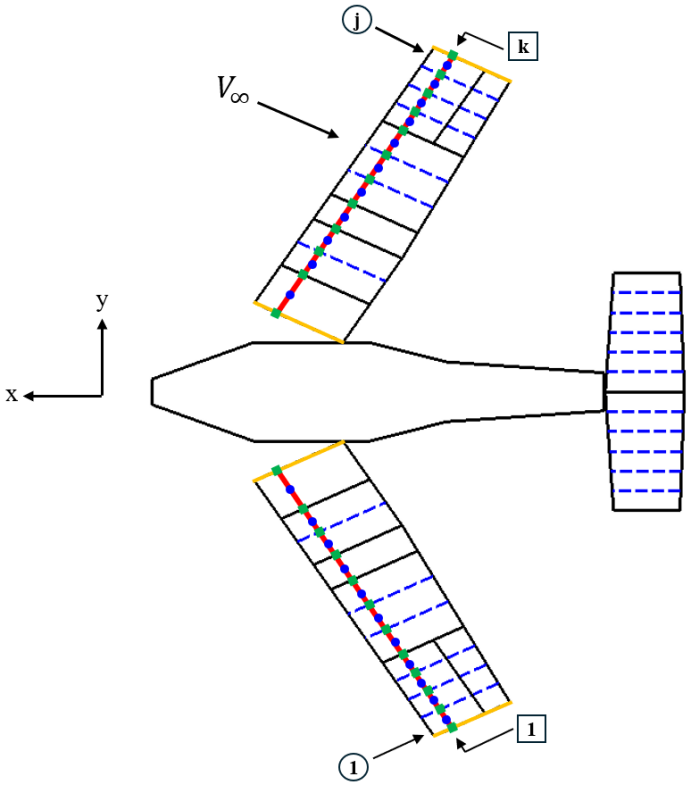


Figure 7 – Transition Configuration and Lifting-Line Panels

Equation (44)-(47) represents the forces and moments computed at each aerodynamic point (LLT_j) on the wing and tail surfaces.

$$L = \sum_{j=1}^{n_p} \rho V_{rel_j} \Gamma_{LLT_j} \cos(\alpha_{ind_j}) \Delta y_{panel_j} \tag{44}$$

$$D = \sum_{j=1}^{n_p} \rho V_{rel_j} \Gamma_{LLT_j} \sin(\alpha_{ind_j}) \Delta y_{panel_j} \tag{45}$$

$$M = \sum_{j=1}^{n_p} \tfrac{1}{2} \rho V_{rel_j}^2 C_{m_j} \bar{c}_j^2 \Delta y_{panel_j} \tag{46}$$

$$F_{LLT_j}^{wing} = \begin{bmatrix} -D \\ 0 \\ -L \end{bmatrix}, \qquad M_{LLT_j}^{wing} = \begin{bmatrix} 0 \\ M \\ 0 \end{bmatrix} \tag{47}$$

The aerodynamic forces and moments are computed in the LLT frame rather than the CG frame. These results are then sequentially rotated into the body and CG frames only, without including translational effects. Since the body and CG frames are parallel with only a positional difference, this transformation can be expressed as in Eqs. (48)–(49).

$$F_{LLT_j}^{CG} = F_{LLT_j}^{B} = C_{wing}^{B} F_{LLT_j}^{wing} \tag{48}$$

$$M_{LLT_j}^{CG} = M_{LLT_j}^{B} = C_{wing}^{B} M_{LLT_j}^{wing} \tag{49}$$

Subsequently, the moments about the center of gravity (CG) are obtained by considering the position vectors from the CG to each LLT_j point, as expressed in $M_{r\times F_{body,j}}^{CG}$.

$$M_{r\times\ F_{body,j}}^{CG} = r_{CG->LLT_j} F_{LLT_j}^{B} \tag{50}$$

This procedure is repeated for all aerodynamic points on both the main wing and tail surfaces. The final aerodynamic force F_{aero} can be obtained according to Eq. (48). Similarly, the total moment can be obtained by first calculating the moment generated by the airfoils, M_{af}, according to Eq. (49), and then summing it with the results of Eq. (50) to yield the final aerodynamic moment as expressed in Eq. (53).

$$F_{aero} = \sum_{j=1}^{n_p} F^{CG}_{LLT_j,wing} + \sum_{j=1}^{n_{Tp}} F^{CG}_{LLT_j,tail} \tag{51}$$

$$M_{af} = \sum_{j=1}^{n_p} M^{CG}_{LLT_j,wing} + \sum_{j=1}^{n_{Tp}} M^{CG}_{LLT_j,tail} \tag{52}$$

$$M_{aero} = M_{af} + \sum_{j=1}^{n_p} M^{CG}_{r\times F_{body,j}} + \sum_{j=1}^{n_{Tp}} M^{CG}_{r\times F_{body,j}} \tag{53}$$

Finally, the total aerodynamic force F_{aero} and moment M_{aero} acting on the aircraft are calculated by summing the contributions from each LLT_j point in the body frame together with the corresponding moment arms relative to the CG. This approach ensures that the resulting forces and moments are expressed in the CG frame.

2.6 Trim Analysis

The trim state of the Folding wing UAV is determined by satisfying equilibrium in both forces and moments. For a given altitude H, airspeed V, and flight-path angle γ, the state vector x and control vector u are iteratively computed until the residuals converge.

The state vector x, containing the attitude variables, and the control vector u, representing control surface deflections and rotor speeds, are given as

$$x = [\alpha, \phi, \theta]^T,\ u = [\delta_a, \delta_e, \delta_r, n_1, n_2, n_3, n_4]^T \tag{54}$$

where α is the angle of attack, ϕ the roll angle, θ the pitch angle, δ's are control-surface deflections, and n_i denote propeller speeds.

The residual vector R is constructed from the resulting force and moment components

$$R(x,u) = \begin{bmatrix} \sum F_x \\ \sum F_y \\ \sum F_z \\ \sum M_x \\ \sum M_y \\ \sum M_z \end{bmatrix} \tag{55}$$

A trim solution is accepted when

$$\|R_F\| \le \varepsilon_f, \quad \|R_M\| \le \varepsilon_m \tag{56}$$

where ε_f and ε_m are convergence tolerances set to 10^{-8} for both force and moment residuals.

In the trim analysis, the total external loads acting on the UAV are decomposed into aerodynamic, propulsive, and gravitational terms as given in Eq. (5), while the total moments are expressed in Eq. (6).

Aerodynamic contributions are evaluated using 3D strip theory

$$[F_{\text{aero}}, M_{\text{aero}}] = f_{\text{aero}}(\rho, V, \alpha, \beta, \delta_a, \delta_e, \delta_r) \tag{57}$$

while propulsive loads are obtained from blade-element momentum theory (BEMT)

$$[F_{\text{prop}}, M_{\text{prop}}] = f_{\text{prop}}(n_i, \rho, V, \alpha, \beta) \tag{58}$$

To enable convergence in both hover and cruise configurations, residual moments are distributed between aerodynamic surfaces and differential thrust using tilt-dependent weighting factors

$$K_{\text{FW}} = g(\gamma_p), \quad K_{\text{MC}} = 1 - K_{\text{FW}} \tag{59}$$

where K_{FW} increases as the wing approaches the cruise configuration, while K_{MC} dominates in hover. The moment balance is then expressed as

$$M_x = K_{\text{FW}} M_{x,\text{aero}} + K_{\text{MC}} M_{x,\text{prop}} \tag{60}$$
$$M_y = K_{\text{FW}} M_{y,\text{aero}} + K_{\text{MC}} M_{y,\text{prop}} \tag{61}$$
$$M_z = K_{\text{FW}} M_{z,\text{aero}} + K_{\text{MC}} M_{z,\text{prop}} \tag{62}$$

Without this allocation, convergence often fails in the transition regime due to conflicting control authority between aerodynamic and propulsive actuators.
At iteration k, the states and controls are corrected using proportional–derivative laws driven by the residuals

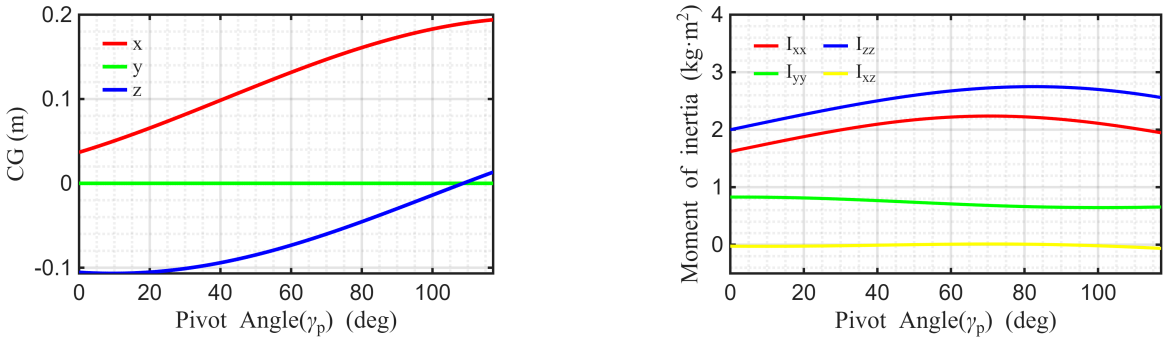
$$\alpha^{(k+1)} = \alpha^{(k)} + K_\alpha R_{Fz} \tag{63}$$
$$\phi^{(k+1)} = \phi^{(k)} + K_\phi R_{Fy} \tag{64}$$
$$\delta_e^{(k+1)} = \delta_e^{(k)} + K_{\delta e} R_{My} \tag{65}$$
$$\delta_a^{(k+1)} = \delta_a^{(k)} + K_{\delta a} R_{Mx} \tag{66}$$
$$\delta_r^{(k+1)} = \delta_r^{(k)} + K_{\delta r} R_{Mz} \tag{67}$$
$$n_i^{(k+1)} = n_i^{(k)} + K_n (R_{Fx}, R_{Fz}, R_M) \tag{68}$$

where $K_\alpha, K_\phi, K_{\delta e}, K_{\delta a}, K_{\delta r}, K_n$ are tuning gains. This scheme can be interpreted as a fixed-point iteration in which control allocation guides the convergence path.
The trim solution is represented as

$$\text{trim} = \{\alpha, \phi, \theta, \delta_a, \delta_e, \delta_r, \delta_f, n_i, P_i\} \tag{69}$$

where P_i denotes the motor power coefficient, derived from the steady-state motor power relations between voltage, current, torque, and rotational speed [14].

3. RESULTS

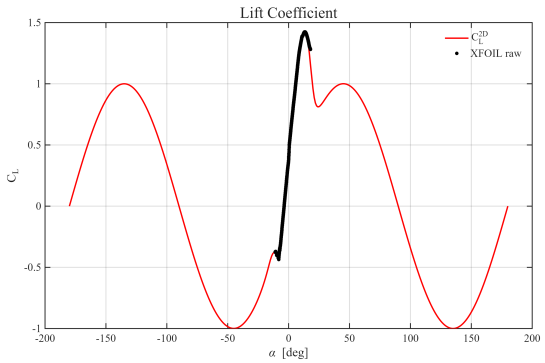


(a) CG variation as a function of pivot angle

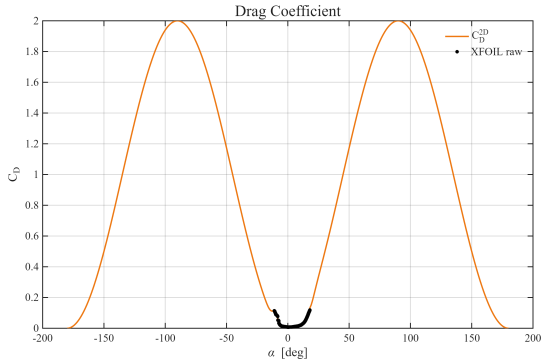
(b) MOI variation as a function of pivot angle

Figure 8 – CG and MOI variations as functions of pivot angle

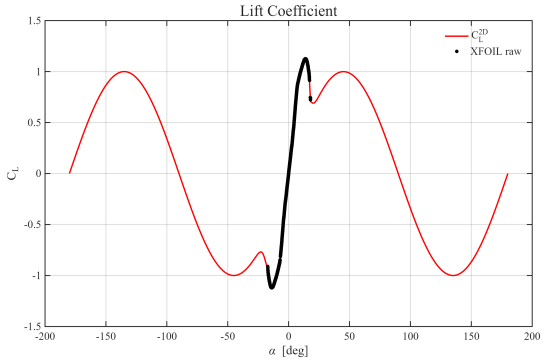
Fig. 8 illustrates the variation of the center of gravity (CG) and the moments of inertia (MOI) with respect to the wing pivot angle γ_p. The results confirm that the CG shifts and inertia trends predicted by the dynamic model are consistent with those obtained from a detailed CAD-based analysis, where material properties were assigned to the three-dimensional geometry to compute mass properties. This agreement validates the reliability of the modeling approach for capturing configuration-dependent changes in mass distribution.
Fig. 9 presents the two-dimensional aerodynamic characteristics of the Clark-Y and NACA0015 airfoils. In the pre-stall regime, the data were obtained using XFOIL, while beyond the stall onset a flat-plate model was applied to extend the angle-of-attack coverage to –180° through 180°.



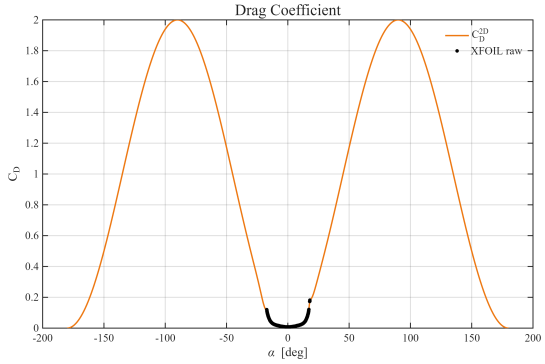
(a) Clarky CL



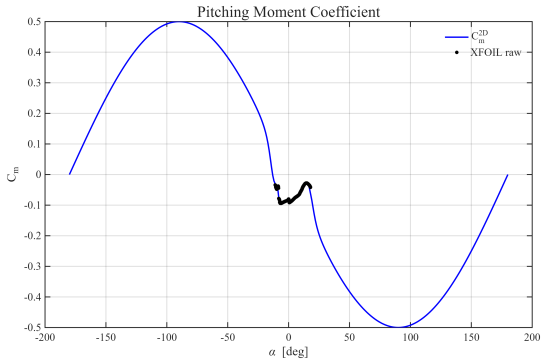
(b) Clarky CD



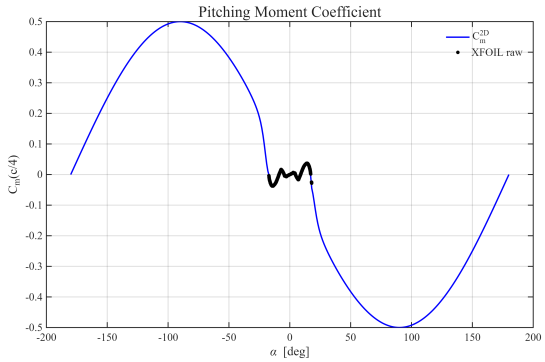
(c) NACA0015 CL



(d) NACA0015 CD



(e) Clarky CM



(f) NACA0015 CM

Figure 9 – 2D Aerodynamic Coefficients of Clark-Y and NACA0015 Airfoils

The resulting coefficients were incorporated into a circulation-based aerodynamic method, enabling the assessment of airfoil performance across the entire nonlinear range of operation. This circulation extension provides accurate prediction of aerodynamic forces and moments in the post-stall domain and is essential for representing the complete operational envelope of the lifting surfaces. Fig. 10 presents the propeller forces and moments predicted by the BEMT model as a function of rotor speed for a forward velocity of $V_\infty = 10$ m/s. Results are presented for selected wing-pivot angles of $\lambda = 0°, 20°, 40°$, and $70°$, representing representative conditions during transition.

The axial force F_x increases nearly linearly with RPM, with a slight amplification at higher inflow angles due to propeller–wing interaction. The vertical force F_z remains negative and becomes more pronounced as λ increases. The rolling moment M_x shows a monotonic decrease with RPM, largely insensitive to inflow angle, whereas the yawing moment M_z exhibits a stronger dependence, becoming increasingly negative with larger λ.

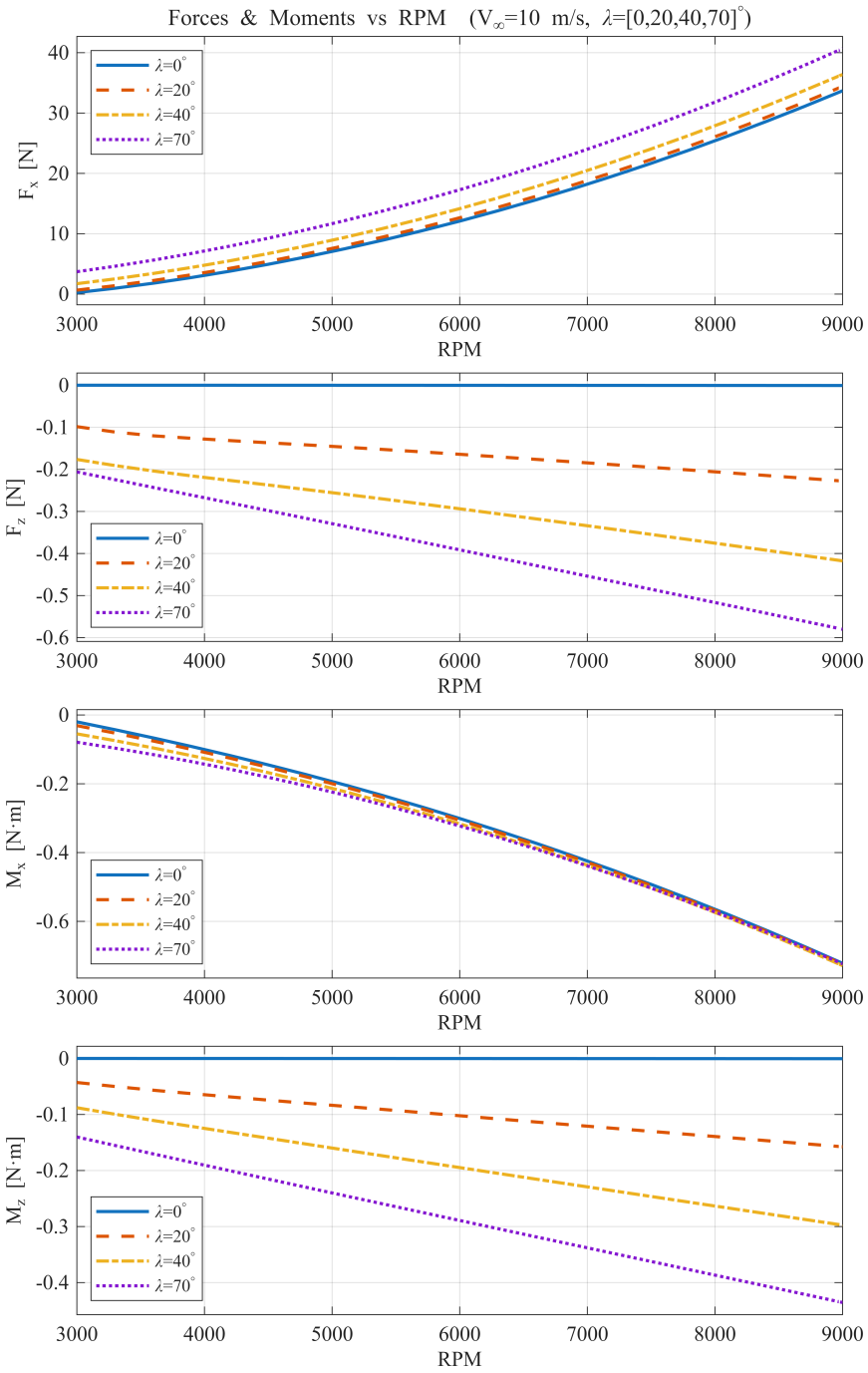


Figure 10 – Propeller forces and moments versus rotor speed at $V_\infty = 10$ m/s for selected inflow angles λ

Table. 1 summarizes the trim speed profile of the Folding wing UAV across different wing-pivot angles. These reference values were obtained from flight-test measurements of the prototype vehicle and subsequently used to define the airspeed parameter V in the trim analysis framework. The results capture the gradual increase in trim speed as the wing transitions from a vertical (hover) orientation to a horizontal (fixed-wing) configuration, with a maximum trim speed of approximately 18 m/s at $\gamma_p = 117°$. The trim state is defined as the flight condition in which the angle of attack α, sideslip angle β, and airspeed V remain constant, while the angular velocity components (p, q, r) are zero. Under these constraints, the net external forces and moments vanish, establishing a steady equilibrium. The results presented in Tables 1 and 2 confirm that this equilibrium is achieved consistently across the entire transition envelope, demonstrating the validity and robustness of the proposed trim analysis framework.

Table 1 – Trim speed profile obtained from flight-test data of the actual vehicle

Pivot angle γ_p [°]	Trim speed V [m/s]
0	0
10	1
20	3
30	4
40	5
50	7
60	8
70	9
80	11
90	13
100	15
110	17
117	18

Table 2 – Trim results of the Folding wing UAV across different pivot angles

Pivot [°]	V [m/s]	α [°]	δ_e [°]	Motor Speeds [RPM]
0	0	0.00	0.00	6417, 5596, 6417, 5596
10	1	4.20	0.00	6407, 5377, 6407, 5377
20	3	6.99	0.00	6513, 5013, 6513, 5013
30	4	7.90	0.00	6608, 4536, 6598, 4546
40	5	7.49	-0.33	6684, 4020, 6675, 4020
50	7	4.37	-1.96	6665, 3619, 6656, 3619
60	8	2.75	-4.55	6426, 3791, 6426, 3791
70	9	1.31	-7.12	5921, 4393, 5930, 4384
80	11	-0.89	-12.89	5433, 4928, 5433, 4918
90	13	-1.51	-3.85	5242, 5242, 5242, 5242
100	15	-0.60	-3.44	5424, 5424, 5424, 5424
110	17	0.92	-3.83	5577, 5577, 5577, 5577
117	18	3.39	-5.43	5634, 5634, 5634, 5634

4. CONCLUSION

In this work, an aerodynamic–propulsive modeling and trim analysis approach for a Folding wing VTOL aircraft was developed. The aerodynamic characteristics of the lifting surfaces were obtained using XFOIL in the pre-stall regime and extended to the full angle-of-attack domain from –180° to 180° through a flat-plate model. These sectional datasets were further processed using a circulation-based formulation and lifting-line corrections, enabling the prediction of nonlinear aerodynamic behavior across both attached-flow and separated-flow conditions. When integrated with a propeller model based on BEMT, the modeling methodology provided a complete description of the forces and moments acting on the vehicle across hover, transition, and fixed-wing modes.

Trim simulations using this model successfully captured the gradual shift of lift generation from rotors to wings, as well as the nonlinear aero–propulsive coupling that dominates the transition regime. The results demonstrate that accurate force and moment equilibrium can be achieved without reliance on wind tunnel data, confirming the effectiveness of the proposed methodology as a tool for early-stage design and analysis of unconventional eVTOL aircraft.

Future work will build upon this model by incorporating a physical prototype of the folding wing UAV. The current aerodynamic and propulsive model will be integrated into a closed-loop flight control simulation, where the simulated vehicle response will be compared with actual flight-test data to evaluate model fidelity. Based on this validation, robust controllers will be designed to ensure stability and controllability across the entire transition envelope. In particular, emphasis will be placed on

achieving seamless maneuverability in all operating modes, from hover to cruise, enabling reliable performance in real-world missions. The combination of high-fidelity modeling, control system integration, and experimental verification will provide a solid foundation for the practical deployment of variable-geometry VTOL platforms.

5. Acknowledgments

This research was supported by the National Research Foundation of Korea (NRF) grant funded by the Ministry of Science and ICT.(No. NRF-2022M1A3B9080233)

6. Copyright Statement

The authors confirm that they, and/or their company or organization, hold copyright on all of the original material included in this paper. The authors also confirm that they have obtained permission, from the copyright holder of any third party material included in this paper, to publish it as part of their paper. The authors confirm that they give permission, or have obtained permission from the copyright holder of this paper, for the publication and distribution of this paper as part of the ICAS proceedings or as individual off-prints from the proceedings.

References

[1] Osita Ugwueze, Thomas Statheros, Mike A Bromfield, and Nadjim Horri. Trends in evtol aircraft development: The concepts, enablers and challenges. In *AIAA Scitech 2023 forum*, page 2096, 2023.

[2] William J Fredericks, David D North, Mark A Agate, and Zachary R Johns. Nasa gl-10 tilt-wing vtol uas flight validation experiments. Technical report, 2015.

[3] David D North, Ronald C Busan, and Greg Howland. Design and fabrication of the la-8 distributed electric propulsion vtol testbed. In *AIAA SciTech 2021 Forum*, page 1188, 2021.

[4] Zehuai Lin, Binbin Yan, Tong Zhang, Shaoyi Li, Zhongjie Meng, and Shuangxi Liu. Multi-level switching control scheme for folding wing vtol uav based on dynamic allocation. *Drones*, 8(7):303, 2024.

[5] Enrico Ajanic, Mir Feroskhan, Valentin Wüest, and Dario Floreano. Sharp turning maneuvers with avian-inspired wing and tail morphing. *Communications Engineering*, 1(34), 2022.

[6] Taeeon Hwang. Optimal takeoff and landing trajectory generation using a tilt profile-guided transition strategy for tiltrotor VTOL UAV. Master's thesis, Korea Aerospace University, Goyang, Republic of Korea, 2024.

[7] Joseph E Sedlak and Babak Vint. Change of inertia tensor due to a severed radial boom for spinning spacecraft. In *AAS/AIAA Astrodynamics Specialist Conference 2018*, number GSFC-E-DAA-TN59694, 2018.

[8] Sanghyuk Park. Blade element momentum method for propeller under nonaxial flow. *International Journal of Aeronautical and Space Sciences*, 24(2):334–340, 2023.

[9] Sean Dougherty. Aerodynamic performance investigations of UAV propellers at low Reynolds number. Master's thesis, University of Canterbury, Department of Mechanical Engineering, Christchurch, New Zealand, 2017.

[10] Björn Montgomerie. Methods for root effects, tip effects and extending the angle of attack range to $\pm 180^\circ$, with application to aerodynamics for blades on wind turbines and propellers. Technical Report FOI-R–1305–SE, Swedish Defence Research Agency (FOI), Stockholm, Sweden, 2004.

[11] Michael S Selig. Real-time flight simulation of highly maneuverable unmanned aerial vehicles. *Journal of Aircraft*, 51(6):1705–1725, 2014.

[12] Jacob Cook. A strip theory approach to dynamic modeling of evtol aircraft. In *AIAA Scitech 2021 Forum*, page 1720, 2021.

[13] Gavin K Ananda and Michael S Selig. Stall/post-stall modeling of the longitudinal characteristics of a general aviation aircraft. In *AIAA Atmospheric Flight Mechanics Conference*, page 3541, 2016.

[14] Jinseok Jeong, Hayoung Shi, Kichang Lee, and Beomsoo Kang. Improvement of electric propulsion system model for performance analysis of large-size multicopter uavs. *Applied Sciences*, 10(22):8080, 2020.